Check for updates

Electrocatalytic oxygen reduction by a Co/Co$_3$O$_4$@N-doped carbon composite material derived from the pyrolysis of ZIF-67/poplar flowers†

Yanling Wu,[a] Yanmin Wang, [ID][a] Zuoxu Xiao,[b] Miantuo Li,[a] Yongling Ding[a] and Mei-li Qi [ID] *[ac]

Catalysts used for the oxygen reduction reaction (ORR) are crucial to fuel cells. However, the development of novel catalysts possessing high activity at a low cost is very challenging. Recently, extensive research has indicated that nitrogen-doped carbon materials, which include nonprecious metals as well as metal-based oxides, can be used as excellent candidates for the ORR. Here, Co/Co$_3$O$_4$@N-doped carbon (NC) with a low cost and highly stable performance is utilized as an ORR electrocatalyst through the pyrolysis of an easily prepared physical mixture containing a cobalt-based zeolite imidazolate framework (ZIF-67 precursor) and biomass materials from poplar flowers. Compared with the pure ZIF-derived counterpart (Co@NC) and PL-bio-C, the as-synthesized electrocatalysts show significantly enhanced ORR activities. The essential roles of doped atoms (ZIF-67 precursor) in improving the ORR activities are discussed. Depending mainly on the formation of Co–Co$_3$O$_4$ active sites and abundant nitrogen-containing groups, the resulting Co/Co$_3$O$_4$@NC catalyst exhibits good electroactivity (onset and half-wave potentials: E_{onset} = 0.94 V and $E_{1/2}$ = 0.85 V, respectively, and a small Tafel slope of 90 mV dec^{-1}) compared to Co@NC and PL-bio-C and follows the 4-electron pathway with good stability and methanol resistance. The results of this study provide a reference for exploring cobalt-based N-doped biomass carbon for energy conversion and storage applications.

1. Introduction

With the development of highly efficient oxygen reduction reaction (ORR) electrocatalysts, rechargeable metal–air batteries and regenerative fuel cells have become more widely used because the cathodic ORR is a rate-limiting process.[1,2] In general, platinum-based catalysts are considered the most active catalysts used for the ORR. They can support the 4-electron pathway even at relatively low overpotentials. However, problems such as anode crossover, high cost, severe intermediate poisoning, and lack of stability under electrochemical conditions are inevitable.[3]

Recently, numerous research efforts have been made to find substitutes for Pt-based catalysts, leading to the development of

novel ORR catalysts at a low cost. The substituting materials that have been reported involve transition-metal chemical compounds,[4,5] N-coordinated metals on the matrices of carbon,[6,7] carbon materials with element doping,[8,9] and even conductive polymers.[10] Among transition-metal oxide-based systems, Co$_3$O$_4$-based electrocatalysts with diverse nanostructures and sizes, such as mesoporous Co$_3$O$_4$,[11] Co$_3$O$_4$ porous sheets,[12] mesoporous Co$_3$O$_4$ nanowires,[13] and Co$_3$O$_4$ nanorods,[14] have gained considerable interest owing to their enhanced electrocatalytic capability, simple preparation procedure, low cost and environmentally friendly characteristics. However, poor electrical conductivity seriously hinders their further application. To date, the most effective way to solve the above problems has been to introduce carbon-based materials as supports, among which porous carbon nanowire arrays,[15] graphene,[16] and carbon nanotubes[17] are the most commonly used. N-doped carbon materials can significantly improve the stability and conductivity of Co$_3$O$_4$-based catalysts.[18] However, the catalysts of Co$_3$O$_4$/C materials tend to peel off substrate surfaces during continuous cycling, exhibiting poor stability. The underlying reason is that the Co$_3$O$_4$/C composites are mainly obtained by directly loading nanoparticles on the surface of carbon.[19,20] As a new precursor, the zeolite

[a]*School of Transportation and Civil Engineering, Shandong Jiaotong University, Ji'nan 250357, China. E-mail: beauty0507@163.com*

[b]*College of Science, China University of Petroleum (East China), Qingdao 266580, China*

[c]*Shandong Branden Medical Devices Co., Ltd, Qihe 251100, China*

† Electronic supplementary information (ESI) available: EDS mapping image; N$_2$ adsorption/desorption isotherm plot of PL-bio-C and Co/Co$_3$O$_4$@NC; XPS survey spectrum of Co/Co$_3$O$_4$@NC; amperometric *i*–*t* curves of Co/Co$_3$O$_4$@NC; and LSV curves of the PL-bio-C and Co@NC catalysts. See DOI: 10.1039/d0ra09615f

imidazolate framework (ZIF-67) has aroused great attention due to its high specific surface area, abundant pores and structural diversity.[21,22] Moreover, during the pyrolysis process, some of the N in the ZIF, which acts as a precursor, can enter the sp^2 lattice of the graphite carbon crystal. Therefore, the electronic structure inside the carbon matrix will be changed, and active chemisorption sites will be created. N, as a heteroatom, is able to produce good synergistic effects by coordinating itself with free metal and functional elements.[23,24]

In this work, we developed a simple route to synthesize Co/Co_3O_4@N-doped active carbon nanostructures (denoted as Co/Co_3O_4@NC) derived from the pyrolysis of a zeolite imidazolate framework (ZIF-67) and the economical, abundant and renewable biomass of poplar flowers. The resulting Co/Co_3O_4@NC catalyst, containing active sites from Co/Co_3O_4 and N-doped carbon, displays excellent ORR activity in 0.1 M KOH (E_{onset} = 0.94 V, $E_{1/2}$ = 0.85 V, as well as a small Tafel slope of 90 mV dec^{-1}), which, *via* a 4-electron pathway, has long-term durability and resistance to methanol poisoning. This absorption-reaction route offers a new approach for synthesizing ZIF materials on conductive substrates.

2. Materials and methods

2.1. Chemicals and characterization methods

Detailed information on the chemical reagents, characterization methods and electrochemical measurements is listed in the ESI.†

2.2. Preparation process of electrocatalysts

In a typical synthesis, the poplar flower (denoted as PL) was first cleaned and dried. Then, 1.0 g of poplar flower powder and 0.05 g of the ZIF-67 precursor were mixed in 20 mL of methanol and stirred for 24 h. The ZIF-67 precursor was synthesized in accordance with a previous reference.[25] The product was dried at 80 °C for 12 h, and after being cooled, the above mixture was uniformly ground. Carbonization was carried out in an inert atmosphere at 10 °C min^{-1} and kept at 800 °C for 3 h. After being cooled, cleaned and dried, the final target sample (named Co/Co_3O_4@NC) was obtained. For comparison purposes, PL-based porous graphite carbon materials (denoted as PL-bio-C) and Co-based N-doped carbon materials derived from the

pyrolysis of ZIF-67 (named Co@NC) were prepared under the same conditions, as shown in Fig. 1.

3. Results and discussion

3.1. Morphological and structural characterization

The morphological and structural details of the obtained electrocatalysts were tested by field-emission scanning electron microscopy (FE-SEM), transmission electron microscopy (TEM) and high-resolution TEM (HR-TEM). Fig. 2 shows the FE-SEM images of PL-bio-C, Co@NC, and Co/Co_3O_4@NC. First, the FE-SEM images show the grooved lamellar structure of the PL-bio-C material (Fig. 2a). The ZIF-67 precursor displays a cubic structure with relatively rough edges (Fig. S1, ESI†). After pyrolysis, the structure of the ZIF-67 precursor remains in Co@NC, but the size of the cubic nanostructure shrinks from 500 to 200 nm (Fig. 2b). As verified by comparison of Fig. 2a and b, the added particles from the ZIF-67 precursor are successfully loaded on the nanoparticles originating from the biomass materials of the poplar flower powder, and the dispersion of these nanoparticles is improved, as shown in Fig. 2c.

The morphology of Co@NC and Co/Co_3O_4@NC was further examined with TEM. The TEM images of the Co@NC (Fig. S2†) display many clustered cube structures of approximately 200 nm, similar to the SEM images. After doping, some small inorganic dots (3 to 5 nm in diameter) were surrounded by a graphite carbon layer (Fig. 3a), suggesting that the active inorganic species were embedded successfully in the carbon material. As shown in Fig. 3b and c, the active species are dispersed on the surface of Co/Co_3O_4@NC. The following d-spacings, 0.34, 0.18, and 0.24 nm, are assigned to the (002) plane of graphite carbon, (200) plane of Co, and (311) plane of Co_3O_4, respectively.[26] The elemental mapping images (Fig. S3, ESI†) further indicate that Co, C, N, and O are distributed homogeneously on the Co/Co_3O_4@NC sample.

The crystal structures of the as-prepared samples, PL-bio-C, Co@NC, and Co/Co_3O_4@NC, were evaluated by powder X-ray diffraction (PXRD) (Fig. 4a). The prepared samples of PL-bio-C and Co/Co_3O_4@NC reveal relatively broad (002) diffraction peaks at approximately 26° and observable characteristic (101) diffraction at ~43°, indicating fairly disordered but chiefly sp^2-hybridized graphitic structures.[27] Relatively sharp peaks from metallic Co (JCPDS no. 15-0806) can be observed except for
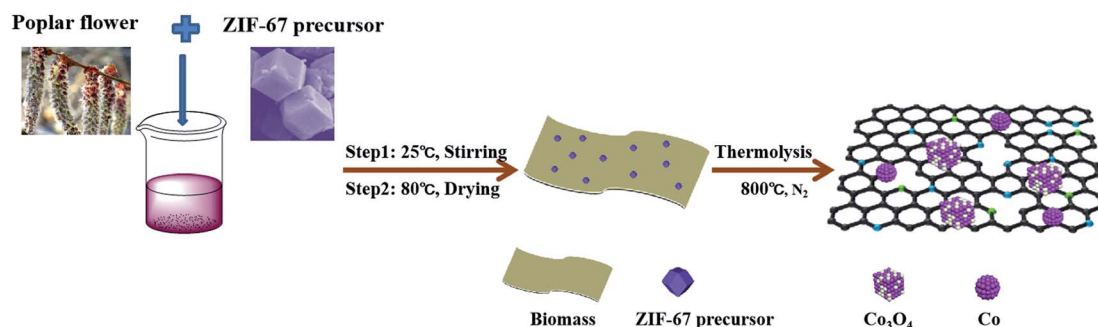

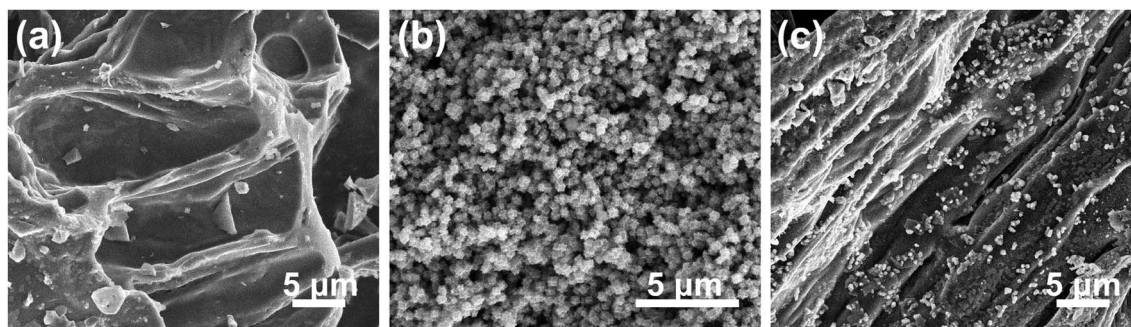**Fig. 1** Schematic diagram showing the synthesis of the Co/Co_3O_4@NC catalytic material.

Fig. 2 Representative FE-SEM images of (a) PL-bio-C, (b) Co@NC, and (c) Co/Co$_3$O$_4$@NC.

a weak carbon peak at approximately 26° in the prepared Co@NC sample. Meanwhile, additional diffraction peaks can be well indexed to metallic Co (JCPDS no. 15-0806) and cubic phase Co$_3$O$_4$ (JCPDS no. 42-1467) detected in the PXRD pattern of Co/Co$_3$O$_4$@NC, suggesting the coexistence of Co and Co$_3$O$_4$ composites on the graphitic matrix of carbon,[28] which is in good accordance with the HR-TEM result mentioned above and the Raman results. The Raman spectra of undoped PL-bio-C and doped Co/Co$_3$O$_4$@NC (Fig. 4b) display two peaks appearing at approximately 1330 and 1590 cm^{-1}, further disclosing the existence of the GC phase in all these PL-bio-C-based materials.[29] In the present case, the low I_D/I_G ratio of graphitic carbon in Co/Co$_3$O$_4$@NC (1.003) compared to that in pure PL-bio-C material (1.065) indicates a relatively high graphitization degree of Co/Co$_3$O$_4$@NC, which should be expected to decrease the barrier to charge transport.[30,31] To further study the surface area of doped and undoped PL-bio-C materials, nitrogen adsorption–desorption isotherms were obtained (Fig. S4 and Table S1, ESI†). The results show that since Co and Co$_3$O$_4$ particles are deposited on PL-bio-C, the surface area of Co/Co$_3$O$_4$@NC (30.38 m^2 g^{-1}) decreases quickly from that of PL-bio-C (201.43 m^2 g^{-1}, Table S4†). The pore width of Co/Co$_3$O$_4$@NC increases slightly compared with that of PL-bio-C, revealing that the Co and Co$_3$O$_4$ particles are uniformly deposited on the PL-bio-C surface instead of blocking the connected channel of PL-bio-C.[32]

X-ray photoelectron spectroscopy (XPS) tests were adopted to examine the surface composition as well as the chemical valence state of Co/Co$_3$O$_4$@NC. The corresponding results are shown in Fig. 5. Distinctive peaks of C, N, O, and Co in the survey spectrum provide the following elemental contents: C (80.61%), N (1.43%), O (17.08%) and Co (0.89%) (Fig. S5†). Furthermore, based on the inductively coupled plasma optical emission spectrometry (ICP-OES) results, the Co content of Co/Co$_3$O$_4$@NC in aqua regia solution (10 mL, 0.0151 g) is 0.7563%. In addition, the comparison of PL-bio-C, Co@NC, and Co/Co$_3$O$_4$@NC survey diagrams found that N was self-doped in the PL-bio-C materials (Fig. S5†). The high-resolution XPS spectrum for C 1s (Fig. 5a) can be divided into 4 peaks centered at 284.5, 284.8, 285.5 and 288.8 eV, which correspond to sp^2-C, sp^3-C, C–N and C=O, respectively. Moreover, the high proportion of sp^2-carbon (C=C at 284.5 eV) further reveals that carbon is in graphitic form, helping to enhance the electron conductivity of carbon materials and improve ORR activity.[33] The fitted N 1s spectra for Co/Co$_3$O$_4$@NC centered at 398.2, 398.9, 400.5, and 401.7 eV in Fig. 5b can be assigned to pyridinic, Co-Nx, pyrrolic, and graphitic nitrogen, respectively. The formation of the Co–N bond is possibly due to the pyrrolic N and pyridinic N affording more negative charges and diffuse orbitals, which are easily used as metal coordination sites to form Co–Nx sites. The robust Co–Nx bonds in the Co/Co$_3$O$_4$@NC electrocatalysts advantageously prevent the migration and agglomeration of nanoparticles.[34] In addition, pyridinic N, graphitic N, and Co–
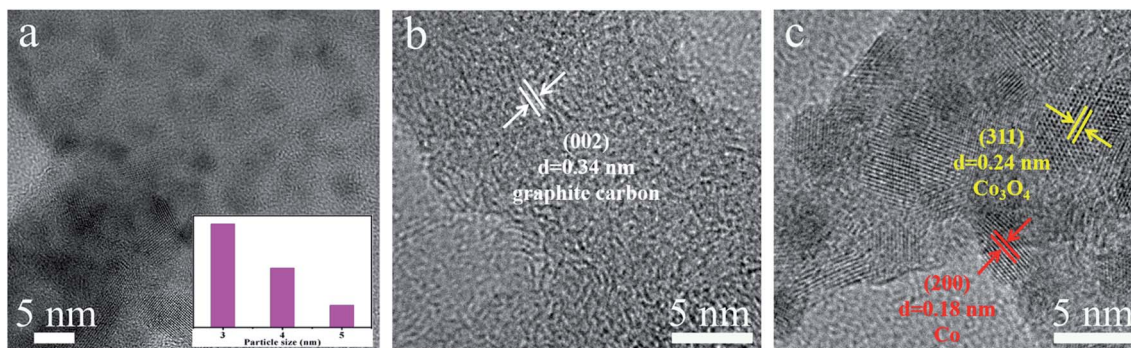

Fig. 3 (a) TEM image of the individual layer of Co/Co$_3$O$_4$@NC (inset shows the particle size distribution of Co/Co$_3$O$_4$@NC). Lattice fringe images of (b) graphitic carbon and (c) Co and Co$_3$O$_4$ taken from the rectangular region, as obtained from the high-resolution TEM of Co/Co$_3$O$_4$@NC.
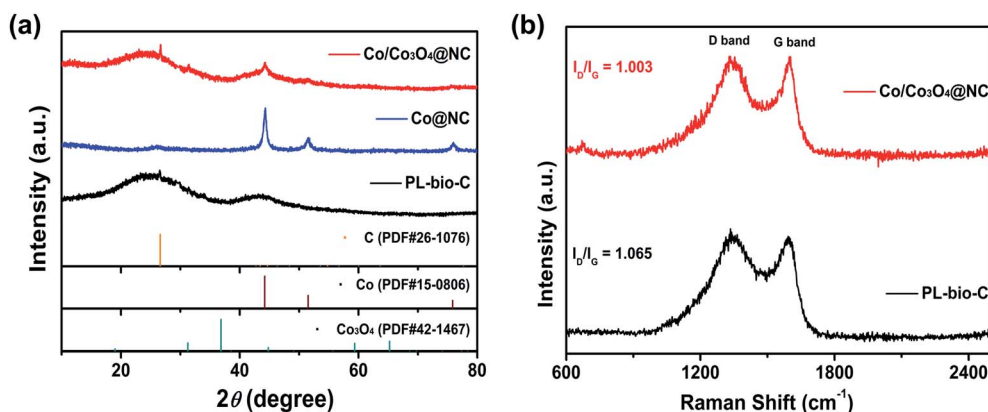
Fig. 4   (a) PXRD patterns of PL-bio-C, Co@NC, and Co/Co$_3$O$_4$@NC and (b) Raman spectra of PL-bio-C and Co/Co$_3$O$_4$@NC.

Nx sites could provide active sites for the ORR, which are advantageous for improving the catalytic ORR activity.[35,36] Furthermore, by comparing the XPS spectrum of N 1 s for PL-bio-C, Co@NC and Co/Co$_3$O$_4$@NC, it was found that there was a high proportion of pyrrolic N in PL-bio-C and a high proportion of Co–Nx in Co@NC. The proportion of pyrrolic N and Co–Nx decreased after the addition of composite materials, which may have a certain influence on the ORR, as shown in Fig. S6.† The XPS spectrum of Co 2p (Fig. 5c) displays 2 core-level signal peaks located at approximately 781.3 and 797.1 eV, which are in agreement with Co 2p$_{3/2}$ and Co 2p$_{1/2}$, respectively. In addition, the ~15.8 eV energy difference

between the Co 2p$_{3/2}$ and Co 2p$_{1/2}$ peaks (named spin–orbit splitting) corresponds well to Co$_3$O$_4$.[37] The two core-level signal peaks can be segmented into seven branch peaks, representative of Co^0 (779.9 eV), Co^{3+} (780.5 eV), Co^{2+} (781.8 and 797.3 eV), Co–Nx (783.7 eV), and 2 shakeup satellites (786.6 and 803.6 eV). Thus, the XPS result confirms the coexistence of Co$_3$O$_4$ and Co in the catalyst. Compared with Co/Co$_3$O$_4$@NC, in addition to the presence of the signal peaks of Co^0 and Co–Nx from the XPS spectrum of Co 2p in the Co@NC (Fig. S7†), there are also Co–O peaks, which are due to the partial oxidation of the Co atomic surface by air.[38] The O 1s region of Co/Co$_3$O$_4$@NC in Fig. 5d can be deconvoluted into three different contributions at 531.4 (O1),
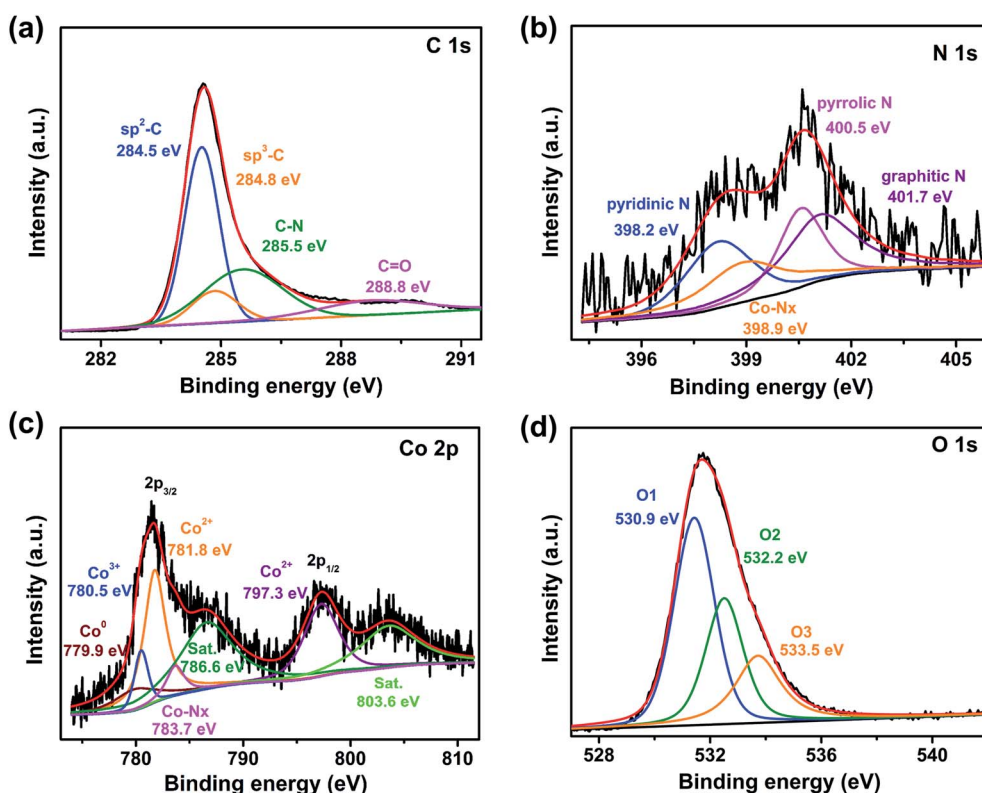

Fig. 5   High-resolution XPS curves of the (a) C 1s, (b) N 1s, (c) Co 2p, and (d) O 1s core levels for Co/Co$_3$O$_4$@NC.

532.5 (O2) and 533.7 eV (O3). The sharp peak at 531.4 eV is attributed to the lattice oxygen (O^{2-}) of Co_3O_4. The peaks at 532.5 and 533.7 eV are caused by oxygen-containing functional groups on the carbon surface.[39]

3.2. Electrochemical properties

First, the electrocatalytic ORR performances of the doped (Co/Co_3O_4@NC), undoped (PL-bio-C) and Co@NC catalysts were successively examined by cyclic voltammetry (CV) in O_2-saturated and N_2-saturated 0.1 M KOH at 50 mV s^{-1} (Fig. 6a and Table S2, ESI†). Compared with the CV of PL-bio-C and Co@NC, the resulting Co/Co_3O_4@NC exhibited enhanced catalytic ORR activity, as evidenced by the shift of the peak potential to a more positive value, further confirming the effectiveness of the material synergy in enhancing the catalytic activity for the ORR.[40]

The ORR activities of the doped and undoped materials were further explored by linear sweep voltammetry (LSV) polarization curves (Fig. 6b). As a comparison, the ORR performance of Co/Co_3O_4@NC is much better than that of undoped PL-bio-C and Co@NC (Fig. 6b, S8, S9 and Table S2, ESI†). The order of ORR activities is PL-bio-C (E_{onset} = 0.81 V, $E_{1/2}$ = 0.63 V, J_L = −3.30 mA cm^{-2}) < Co@NC (E_{onset} = 0.87 V, $E_{1/2}$ = 0.68 V, J_L = −3.86 mA cm^{-2}) < Co/Co_3O_4@NC (E_{onset} = 0.94 V, $E_{1/2}$ = 0.85 V, J_L = −4.78 mA cm^{-2}), indicating that the properties of the catalysts can be successfully improved by further treating the PL-bio-C

materials, although the Brunauer–Emmett–Teller (BET) surface area of Co/Co_3O_4@NC is lower than that of PL-bio-C (Table S1, ESI†). In accordance with the CV study, the LSV curves reveal that Co/Co_3O_4@NC displays a high onset potential (E_{onset}) of 0.94 V and a high half-wave potential ($E_{1/2}$) of 0.85 V. Though the limiting current density of 4.78 mA cm^{-2} for Co/Co_3O_4@NC is much lower than that of Pt/C, Co/Co_3O_4@NC exhibits better ORR performance than most of the electro-catalysts reported in the literature (Table S3†).

To further reveal the advantages of Co/Co_3O_4@NC, LSV curves were obtained at various rotation speeds (400 to 2025 rpm), and the results are shown in Fig. 6c. The current density increases with increasing rotation speed. The Koutecky–Levich (K–L) plots illustrate that the electron transfer number (3.82) for Co/Co_3O_4@NC (inset of Fig. 6c) is higher than those for Co@NC (3.37) and PL-bio-C (2.69). This value is close to the value (4.0) observed with Pt/C (Fig. 6c, S8, S9, and Table S2†), implying that Co/Co_3O_4@NC follows the four-electron oxygen reduction path for the ORR.[41] Fig. 6d shows that the Tafel slope of the doped Co/Co_3O_4@NC (90 mV dec^{-1}) is the smallest in comparison with that of Co@NC (216 mV dec^{-1}), PL-bio-C (251 mV dec^{-1}) and Pt/C (97 mV dec^{-1}), indicating the fast electron transfer rate of the Co/Co_3O_4@NC catalyst.

In an attempt to understand the much improved ORR activity on Co/Co_3O_4@NC, the double layer capacitance (C_{dl}) in the faradaic silent region provided an indication of the
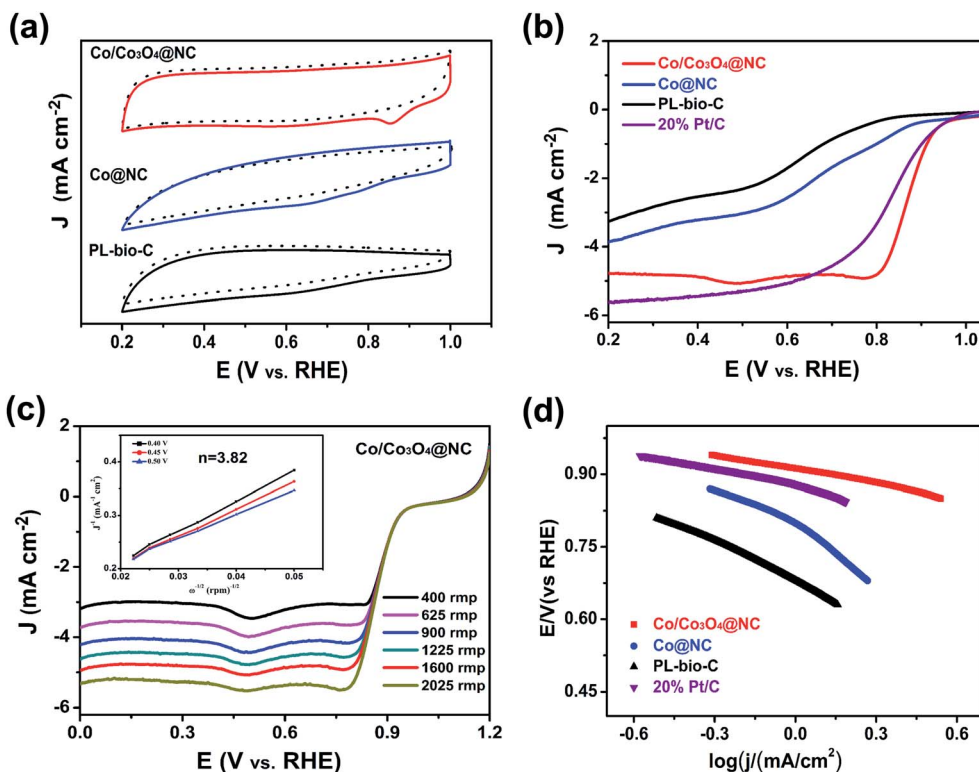

Fig. 6 (a) CV curves of PL-bio-C, Co@NC, and Co/Co_3O_4@NC in 0.1 M KOH at 50 mV s^{-1} (O_2-saturated with solid lines and N_2-saturated with dotted lines). (b) LSV curves of the as-obtained carbon catalysts and commercial 20 wt% Pt/C catalyst in O_2-saturated 0.1 M KOH electrolyte (sweep rate: 10 mV s^{-1} and rotation speed: 1600 rpm). (c) LSV curves of Co/Co_3O_4@NC at multiple rotation speeds. (inset: K–L plots of Co/Co_3O_4@NC at multiple potentials). (d) Tafel plots of PL-bio-C, Co@NC, Co/Co_3O_4@NC, and 20% Pt/C obtained via the LSV data.

electrochemical active surface area (ECSA). The CV curves recorded in nitrogen purged 0.1 M KOH aqueous solution in the potential range from 0.0.5 to 0.15 V (Fig. S10a–c†). The evaluated C_{dl} values for Co/Co$_3$O$_4$@NC, Co@NC and PL-bio-C were 3.62, 1.39 and 2.28 mF cm^{-2} (Fig. S10d†), respectively, which indicated the presence of large amounts of electrochemical active centers in these materials; hence, Co/Co$_3$O$_4$@NC had better activity for the ORR in 0.1 M alkaline solution.[42]

In practice, long-term durability is an important criterion for ORR catalysts with high efficiency. Here, a chronoamperometric response was obtained to measure the stability of Co/Co$_3$O$_4$@NC and Pt/C in O$_2$-saturated 0.1 M KOH. The constant voltage and rotation rate were set at 0.8 V and 1600 rpm, respectively. Co/Co$_3$O$_4$@NC shows 75% retention of the initial current density over 10 000 s of continuous operation, while the Pt/C catalyst undergoes activity loss with only approximately 60% retention (Fig. S11a, ESI†). Consequently, the abundant nitrogen species in Co/Co$_3$O$_4$@NC may provide stable anchoring sites for the Co and Co$_3$O$_4$ active components, thus improving the dispersibility and stability of the active components on this carbon carrier.[39,43,44] Moreover, the methanol crossover experiment shows that the current density has no obvious interference on Co/Co$_3$O$_4$@NC when methanol is added to the electrolyte. In contrast, the Pt/C catalyst displays a sharp decrease in the current as a result of methanol oxidation (Fig. S11b, ESI†). Moreover, the chemical compositions and morphology of Co/Co$_3$O$_4$@NC after ORR long-term stability measurements were also investigated. The XRD patterns of Co/Co$_3$O$_4$@NC show diffraction peaks similar to the original peaks, proving that the chemical components of Co/Co$_3$O$_4$@NC were not transformed after the durability measurement and thus demonstrated excellent electrochemical stability (Fig. S12†). In the XPS spectrum of Co 2p, the ratios of Co 2p$_{3/2}$ and Co 2p$_{1/2}$ peaks respectively located at approximately 781.3 and 797.1 eV for Co/Co$_3$O$_4$@NC decreased from the initial ratio of 1.07/1 to 1.02/1. Otherwise, the initial sharp peak of Co/Co$_3$O$_4$@NC for O 1s at 531.7 eV moves toward a higher energy region (532.5 eV) after the ORR durability test, and a new peak at approximately 532.5 eV likely belongs to chemisorbed oxygen, which confirms the formation of Co(III)OOH on the surface of Co/Co$_3$O$_4$@NC (Fig. S13†).[45] In addition, after the stability test, samples of the Co/Co$_3$O$_4$@NC catalyst were collected, and SEM data indicated that its morphological structure could still be maintained (as shown in Fig. S14†). These results indicate that Co/Co$_3$O$_4$@NC possesses higher ORR catalytic stability and better methanol resistance than the Pt/C catalyst. Furthermore, the reported Co/Co-based oxide electrocatalysts and their catalytic performances for the ORR are summarized in Table S3.† We can infer from Table S3† that the ORR electrocatalytic properties of Co/Co$_3$O$_4$@NC are no less than those of other Co/Co-based oxide-based electrocatalysts, demonstrating its superior catalytic activity.

4. Conclusions

In summary, we developed a low-cost and highly stable Co/Co$_3$O$_4$@NC catalyst for the ORR; Co–Co$_3$O$_4$ provided the active sites, earth-abundant poplar flowers were the carbon source and a zeolite imidazolate framework (ZIF-67) was the precursor. The doped atoms played significant roles in improving the ORR activity of the prepared electrocatalysts. This catalyst exhibited outstanding catalytic activities in 0.1 M KOH ($E_{onset} = 0.94$ V, $E_{1/2} = 0.85$ V, and a small Tafel slope of 90 mV dec^{-1}), which, via a 4-electron pathway, had excellent stability and methanol resistance and was better than those of most currently reported cobalt-based catalysts. The unique Co–Co$_3$O$_4$ nanoparticles as well as N-containing functional groups in the Co/Co$_3$O$_4$@NC catalyst could provide abundant active sites to improve the interfacial electron transfer in the ORR system, thus enhancing the catalytic activity for the ORR. This work offers a cost-effective and scalable pathway to optimize the ORR performance of ZIF-derived electrocatalysts and an intriguing strategy to use sustainable and abundant biomass resources to design nonprecious carbon electrocatalysts.

Author contributions

Writing—original draft and writing—review & editing, Y.-l. W.; investigation, L.-m. T.; data curation, Y.-l. D.; supervision, Z.-x. X.; funding acquisition, Y.-m. W.; resources, M.-l. Q. All authors have read and agreed to the published version of the manuscript.

Conflicts of interest

There are no conflicts to declare.

Acknowledgements

References

1 N. Ma, Y. Jia, X. F. Yang, X. L. She, L. Z. Zhang, Z. Peng, X. D. Yao and D. J. Yang, Seaweed biomass derived (Ni,Co)/CNT nanoaerogels: efficient bifunctional electrocatalysts for oxygen evolution and reduction reactions, *J. Mater. Chem. A*, 2016, **4**, 6376–6384.

2 Z. Y. Chen, Q. C. Wang, X. B. Zhang, Y. P. Lei, W. Hu, Y. Luo and Y. B. Wang, N-doped defective carbon with trace Co for efficient rechargeable liquid electrolyte-/all-solid-state Zn-air batteries, *Sci. Bull.*, 2018, **63**, 548–555.

3 J. C. Meier, C. Galeano, I. Katsounaros, A. A. Topalov, A. Kostka, F. Schüth and K. J. J. Mayrhofer, Degradation mechanisms of Pt/C fuel cell catalysts under simulated start-stop conditions, *ACS Catal.*, 2012, **2**, 832–843.

4 J. Suntivich, H. A. Gasteiger, N. Yabuuchi, H. Nakanishi, J. B. Goodenough and Y. Shao-Horn, Design principles for

oxygen-reduction activity on perovskite oxide catalysts for fuel cells and metal–air batteries, *Nat. Chem.*, 2011, **3**, 546–550.

5 Z. Y. Wu, P. Chen, Q. S. Wu, L. F. Yang, Z. Pan and Q. Wang, Co/Co_3O_4/C–N, a novel nanostructure and excellent catalytic system for the oxygen reduction reaction, *Nano Energy*, 2014, **8**, 118–125.

6 G. Wu, K. L. More, C. M. Johnston and P. Zelenay, High-performance electrocatalysts for oxygen reduction derived from polyaniline, iron, and cobalt, *Science*, 2011, **332**, 443–447.

7 M. Lefevre, E. Proietti, F. Jaouen and J. P. Dodelet, Iron-based catalysts with improved oxygen Reduction Activity in polymer electrolyte fuel cells, *Science*, 2009, **324**, 71–74.

8 K. P. Gong, F. Du, Z. H. Xia, M. Durstock and L. M. Dai, Nitrogen-doped carbon nanotube arrays with high electrocatalytic activity for oxygen reduction, *Science*, 2009, **323**, 760–764.

9 R. L. Liu, D. Q. Wu, X. L. Feng and K. Mullen, Nitrogen-doped ordered mesoporous graphitic arrays with high electrocatalytic activity for oxygen reduction, *Angew. Chem., Int. Ed.*, 2010, **49**, 2565–2568.

10 B. Winther-Jensen, O. Winther-Jensen, M. Forsyth and D. R. MacFarlane, High rates of oxygen reduction over a vapor phase–polymerized PEDOT electrode, *Science*, 2008, **321**, 671–674.

11 Y. J. Sa, K. Kwon, J. Y. Cheon, F. Kleitz and S. H. Joo, Ordered mesoporous Co_3O_4 spinels as stable, bifunctional, noble metal-free oxygen electrocatalysts, *J. Mater. Chem. A*, 2013, **1**, 9992–10001.

12 Y. Sun, S. Gao, F. Lei, J. Liu, L. Liang and Y. Xie, Atomically-thin non-layered cobalt oxide porous sheets for highly efficient oxygen-evolving electrocatalysts, *Chem. Sci.*, 2014, **5**, 3976–3982.

13 Y. Li, B. Tan and Y. Wu, Mesoporous Co_3O_4 nanowire arrays for lithium ion batteries with high capacity and rate capability, *Nano Lett.*, 2008, **8**, 265–270.

14 J. Xu, P. Gao and T. S. Zhao, Non-precious Co_3O_4 nanorod electrocatalyst for oxygen reduction reaction in anion-exchange membrane fuel cells, *Energy Environ. Sci.*, 2012, **5**, 5333–5339.

15 T. Y. Ma, S. Dai, M. Jaroniec and S. Z. Qiao, Metal–organic framework derived hybrid Co_3O_4-carbon porous nanowire arrays as reversible oxygen evolution electrodes, *J. Am. Chem. Soc.*, 2014, **136**, 13925–13931.

16 Y. E. Liang, Y. G. Li, H. L. Wang, J. G. Zhou, J. Wang, T. Regier and H. J. Dai, Co_3O_4 nanocrystals on graphene as a synergistic catalyst for oxygen reduction reaction, *Nat. Mater.*, 2011, **10**, 780–786.

17 S. Zhao, B. Rasimick, W. Mustain and H. Xu, Highly durable and active Co_3O_4 nanocrystals supported on carbon nanotubes as bifunctional electrocatalysts in alkaline media, *Appl. Catal., B*, 2017, **203**, 138–145.

18 A. A. Zhang, J. F. Wu, L. Xue, S. Yan and S. H. Zeng, Probing heteroatomic dopant-activity synergy over Co_3O_4/doped carbon nanotube electrocatalysts for oxygen reduction reaction, *Inorg. Chem.*, 2020, **59**, 403–414.

19 X. Y. Lu, H. M. Chan, C.-L. Sun, C.-M. Tseng and C. Zhao, Interconnected core–shell carbon nanotube–graphene nanoribbon scaffolds for anchoring cobalt oxides as bifunctional electrocatalysts for oxygen evolution and reduction, *J. Mater. Chem. A*, 2015, **3**, 13371–13376.

20 K. Kumar, C. Canaff, J. Rousseau, S. Arrii-Clacens, T. W. Napporn, A. Habrioux and K. B. Kokoh, Effect of the oxide–carbon heterointerface on the activity of Co_3O_4/NRGO Nanocomposites toward ORR and OER, *J. Phys. Chem. C*, 2016, **120**, 7949–7958.

21 M. S. Tehrani and R. Zare-Dorabei, Highly efficient simultaneous ultrasonic-assisted adsorption of methylene blue and rhodamine B onto metal organic framework MIL-68(Al): central composite design optimization, *RSC Adv.*, 2016, **6**, 27416–27425.

22 Q. X. Lai, J. J. Zhu, Y. X. Zhao, Y. Y. Liang, J. P. He and J. H. Chen, MOF-based metal-doping-induced synthesis of hierarchical porous Cu–N/C oxygen reduction electrocatalysts for Zn-air batteries, *Small*, 2017, **13**, 1700740.

23 S. Dou, X. Y. Li, L. Tao, J. Huo and S. Y. Wang, Cobalt nanoparticle-embedded carbon nanotube/porous carbon hybrid derived from MOF-encapsulated Co_3O_4 for oxygen electrocatalysis, *Chem. Commun.*, 2016, **52**, 9727–9730.

24 H. Tabassum, A. Mahmood, Q. F. Wang, W. Xia, Z. B. Liang, B. Qiu, R. Zhao and R. Q. Zou, Hierarchical cobalt hydroxide and B/N Co-doped graphene nanohybrids derived from metal-organic frameworks for high energy density asymmetric supercapacitors, *Sci. Rep.*, 2017, **7**, 43084.

25 R. X. Liang, A. J. Hu, M. L. Li, Z. Q. Ran, C. Z. Shu and J. P. Long, Cobalt encapsulated within porous MOF-derived nitrogen-doped carbon as an efficient bifunctional electrocatalyst for aprotic lithium-oxygen battery, *J. Alloys Compd.*, 2019, **810**, 151877.

26 H. F. Peng, W. L. Zhang, Y. Song, F. X. Yin, C. W. Zhang and L. Zhang, In situ construction of Co/Co_3O_4 with N-doped porous carbon as a bifunctional electrocatalyst for oxygen reduction and oxygen evolution reactions, *Catal. Today*, 2019, DOI: 10.1016/j.cattod.2019.05.003.

27 B. B. Huang, Y. C. Liu and Z. L. Xie, Biomass derived 2D carbons via a hydrothermal carbonization method as efficient bifunctional ORR/HER electrocatalysts, *J. Mater. Chem. A*, 2017, **5**, 23481–23488.

28 C. W. Zhang, Y. Peng, Y. Song, J. J. Li, F. X. Yin and Y. Yuan, Periodic three-dimensional nitrogen-doped mesoporous carbon spheres embedded with Co/Co_3O_4 nanoparticles toward microwave absorption, *ACS Appl. Mater. Interfaces*, 2020, **12**, 24102–24111.

29 W. J. Zhou, T. L. Xiong, C. H. Shi, J. Zhou, K. Zhou, N. W. Zhu, L. G. Li, Z. H. Tang and S. W. Chen, Bioreduction of precious metals by microorganism: efficient gold@N-doped carbon electrocatalysts for the hydrogen evolution reaction, *Angew. Chem.*, 2016, **55**, 8416–8420.

30 H.-K. Jeong, Y. P. Lee, R. J. W. E. Lahaye, M.-H. Park, K. H. An, I. J. Kim, C. W. Yang, C. Y. Park, R. S. Ruoff and Y. H. Lee, Evidence of graphitic AB stacking order of graphite oxides, *J. Am. Chem. Soc.*, 2008, **130**, 1362–1366.

31 J. H. Hou, C. B. Cao, F. Idrees and X. L. Ma, Hierarchical porous nitrogen-doped carbon nanosheets derived from silk for ultrahigh-capacity battery anodes and supercapacitors, *ACS Nano*, 2015, **9**, 2556–2564.

32 X. W. Zhong, W. D. Yi, Y. J. Qu, L. Z. Zhang, H. Y. Bai, Y. M. Zhu, J. Wan, S. Chen, M. Yang, L. Huang, M. Gu, H. Pan and B. M. Xu, Co single-atom anchored on Co_3O_4 and nitrogen-doped active carbon toward bifunctional catalyst for zinc-air batteries, *Appl. Catal., B*, 2020, **260**, 118188.

33 K. L. Ai, Y. L. Liu, C. P. Ruan, L. H. Lu and G. Q. Lu, Sp^2 C-dominant N-doped carbon sub-micrometer spheres with a tunable size: a versatile platform for highly efficient oxygen-reduction catalysts, *Adv. Mater.*, 2013, **25**, 998–1003.

34 Y. Jia, Y. Wang, G. Zhang, C. Zhang, K. Sun, X. Xiong, J. Liu and X. Sun, Pyrolysis-free formamide-derived N-doped carbon supporting atomically dispersed cobalt as high-performance bifunctional oxygen electrocatalyst, *J. Energy Chem.*, 2020, **49**, 283–290.

35 Z. Zhang, J. H. Hao, W. S. Yang and J. L. Tang, Defect-rich CoP/nitrogen-doped carbon composites derived from a metal-organic framework: high performance electrocatalysts for the hydrogen evolution reaction, *ChemCatChem*, 2015, **7**, 1920–1925.

36 Y. J. Zhang, L. H. Lu, S. Zhang, Z. Z. Lv, D. T. Yang, J. H. Liu, Y. Chen, X. C. Tian, H. Y. Jin and W. G. Song, Biomass chitosan derived cobalt/nitrogen doped carbon nanotubes for the electrocatalytic oxygen reduction reaction, *J. Mater. Chem. A*, 2018, **6**, 5740–5745.

37 X. H. Lv, Y. L. Chen, Y. L. Wu, H. Y. Wang, X. L. Wang, C. Y. Wei, Z. X. Xiao, G. W. Yang and J. Z. Jiang, A Br-regulated transition metal active-site anchoring and exposure strategy in biomass-derived carbon nanosheets for obtaining robust ORR/HER electrocatalysts at all pH values, *J. Mater. Chem. A*, 2019, **7**, 27089–27098.

38 X. K. Wang, H. Y. Gai, Z. K. Chen, Y. H. Liu, J. J. Jingjing Zhang, B. L. Bolin Zhao, A. Toghan and M. H. Huang, The marriage of crystalline/amorphous Co/Co_3O_4 heterostructures with N-doped hollow carbon spheres: efficient and durable catalysts for oxygen reduction, *Mater. Today Energy*, 2020, **18**, 100497.

39 J. Masa, W. Xia, I. Sinev, A. Q. Zhao, Z. Y. Sun, S. Grützke, P. Weide, M. Muhler and W. Schuhmann, Mn_xO_y/NC and Co_xO_y/NC nanoparticles embedded in a nitrogen doped carbon matrix for high-performance bifunctional oxygen electrodes, *Angew. Chem., Int. Ed.*, 2014, **53**, 8508–8512.

40 Z. D. Huang, J. H. Liu, Z. Y. Xiao, H. Fu, W. D. Fan, B. Xu, B. Dong, D. Liu, F. N. Dai and D. F. Sun, A MOF-derived coral-like NiSe@NC nanohybrid:an efficient electrocatalyst for the hydrogen evolution reaction at all pH values, *Nanoscale*, 2018, **10**, 22758–22765.

41 D. W. Wang and D. S. Su, Heterogeneous nanocarbon materials for oxygen reduction reaction, *Energy Environ. Sci.*, 2014, **7**, 576–591.

42 Z. H. Li, M. F. Shao, L. Zhou, R. K. Zhang, C. Zhang, M. Wei, D. G. Evans and X. Duan, Directed growth of metal-organic frameworks and their derived carbon-based network for efficient electrocatalytic oxygen reduction, *Adv. Mater.*, 2016, **28**, 2337–2344.

43 Y. Tong, P. Z. Chen, T. P. Zhou, K. Xu, W. S. Chu, C. Z. Wu and Y. Xie, A bifunctional hybrid electrocatalyst for oxygen reduction and evolution: cobalt oxide nanoparticles strongly coupled to B, N-decorated graphene, *Angew. Chem., Int. Ed.*, 2017, **56**, 7121–7125.

44 W. Chaikittisilp, N. L. Torad, C. L. Li, M. Imura, N. Suzuki, S. Ishihara, K. Ariga and Y. Yamauchi, Synthesis of nanoporous carbon-cobalt-oxide hybrid electrocatalysts by thermal conversion of metal-organic frameworks, *Chem.– Eur. J.*, 2014, **20**, 4217–4221.

45 S. X. Yang, W. P. Zhu, Z. P. Jiang, Z. X. Chen and J. B. Wang, The surface properties and the activities in catalytic wet air oxidation over CeO_2–TiO_2 catalysts, *Appl. Surf. Sci.*, 2006, **252**, 8499–8505.